systems by seamless integration of transcriptor logic elements within natural operons). Also, by separating gate inputs from gate control signals and by using a strong input signal modulated by an efficient asymmetric terminator, we were able to demonstrate and quantify signal amplification for all gates (Figs. 3 and 4).

Output signal levels vary within and among the gates reported here (Figs. 2 and 3 and figs. S9 and S10), although not more so than existing genetic logic. We believe that most variation arises from differences in RNA secondary structures well known to influence mRNA stability and translation initiation rates (fig. S15); such variation might be eliminated by using recently reported mRNA processing methods (*24*, *27*). Further work is also required to realize precise level matching across all gates, and directed evolution of increasingly asymmetric terminators may be needed to reduce low output levels for most gates (fig. S10); additional gate-specific tuning of NAND would be required given its noncanonical logic element. Nevertheless, existing gates already support single-layer programmable digital logic, control-signal amplification, sequential logic, and cell-cell communication of intermediate logic states. Multi-input gates supporting high "fan-in" could be realized by using additional integrases (*28*) (fig. S16). Transcriptor-based gates can also likely be directly combined with other logic families to expand the power of engineered genetic computers. All logic gates and uses thereof demonstrated or disclosed here have been contributed to the public domain via the BioBrick Public Agreement (*29*).

References and Notes

1. B. Wang, M. Buck, *Trends Microbiol.* **20**, 376 (2012).
2. Y. Benenson, *Nat. Rev. Genet.* **13**, 455 (2012).
3. T. Miyamoto, S. Razavi, R. DeRose, T. Inoue, *ACS Synth. Biol.* **2**, 72 (2013).
4. D. R. Burrill, P. A. Silver, *Cell* **140**, 13 (2010).
5. J. Bonnet, P. Subsoontorn, D. Endy, *Proc. Natl. Acad. Sci. U.S.A.* **109**, 8884 (2012).
6. S. Basu, Y. Gerchman, C. H. Collins, F. H. Arnold, R. Weiss, *Nature* **434**, 1130 (2005).
7. M. E. Ortiz, D. Endy, *J. Biol. Eng.* **6**, 16 (2012).
8. Y. Y. Chen, M. C. Jensen, C. D. Smolke, *Proc. Natl. Acad. Sci. U.S.A.* **107**, 8531 (2010).
9. Z. Xie, L. Wroblewska, L. Prochazka, R. Weiss, Y. Benenson, *Science* **333**, 1307 (2011).
10. A. Tamsir, J. J. Tabor, C. A. Voigt, *Nature* **469**, 212 (2011).
11. T. S. Moon, C. Lou, A. Tamsir, B. C. Stanton, C. A. Voigt, *Nature* **491**, 249 (2012).
12. S. Ausländer, D. Ausländer, M. Müller, M. Wieland, M. Fussenegger, *Nature* **487**, 123 (2012).
13. For example, converting a NOR gate repressed by transcription factors to an OR gate activated by transcription factors requires changing how proteins interact with RNA polymerase (from competitive binding and occlusion to recruitment and initiation) and simultaneous reworking of the basal activity for core promoter elements (from a constitutively active promoter that can be repressed to a weak promoter that does not spontaneously initiate transcription yet that transcription factors activate).
14. C. Wadey, I. Deese, D. Endy, "Common signal carriers," in *Adventures in Synthetic Biology* (OpenWetWare and Nature Publishing Group New York, 2005), chap. 3; available online at http://hdl.handle.net/1721.1/46337.
15. T. S. Ham, S. K. Lee, J. D. Keasling, A. P. Arkin, *PLoS ONE* **3**, e2815 (2008).
16. A. E. Friedland *et al.*, *Science* **324**, 1199 (2009).
17. P. A. Varadarajan, D. Del Vecchio, *IEEE Trans. Nanobioscience* **8**, 281 (2009).
18. J. Bardeen, W. Brattain, *Phys. Rev.* **74**, 230 (1948).
19. With transistor-based logic, gates use a base, emitter, and collector architecture that classically only allows for control of electrical current at one point on a wire by a single signal. Transcriptor-based logic allows RNA polymerase flow at a single point on DNA to be controlled, in theory, by as many independent recombinases as needed.
20. J. A. Lewis, G. F. Hatfull, *Nucleic Acids Res.* **29**, 2205 (2001).
21. W. R. A. Brown, N. C. O. Lee, Z. Xu, M. C. M. Smith, *Methods* **53**, 372 (2011).
22. B. Canton, A. Labno, D. Endy, *Nat. Biotechnol.* **26**, 787 (2008).
23. Materials and methods are available as supplementary materials on *Science* Online.
24. C. Lou, B. Stanton, Y.-J. Chen, B. Munsky, C. A. Voigt, *Nat. Biotechnol.* **30**, 1137 (2012).
25. L. Pasotti, N. Politi, S. Zucca, M. G. Cusella De Angelis, P. Magni, *PLoS ONE* **7**, e39407 (2012).
26. P. Siuti, J. Yazbek, T. K. Lu, *Nat. Biotechnol.* (2013).
27. L. Qi, R. E. Haurwitz, W. Shao, J. A. Doudna, A. P. Arkin, *Nat. Biotechnol.* **30**, 1002 (2012).
28. G. F. Hatfull *et al.*, *J. Virol.* **86**, 2382 (2012).
29. https://biobricks.org/bpa/

Acknowledgments: We thank M. Juul, T. Knight, S. Kushner, C. Smolke, B. Townshend, the Endy and Smolke labs, and the Stanford Shared FACS Facility. Funding was provided by the NSF Synthetic Biology Engineering Research Center, Stanford Center for Longevity, Stanford Bio-X, the Townshend/Lamarre Family Foundation, and the Siebel Foundation. DNA sequences are available in GenBank (accession nos. KC529324 to KC529332). DNA constructs will be made available via Addgene.

Supplementary Materials

www.sciencemag.org/cgi/content/full/science.1232758/DC1
Materials and Methods
Figs. S1 to S15
Appendices S1 to S4
References (*30*–*44*)
Movie S1

14 November 2012; accepted 13 March 2013
Published online 28 March 2013;
10.1126/science.1232758

Downloaded from www.sciencemag.org on May 3, 2013

Controlled Flight of a Biologically Inspired, Insect-Scale Robot

Kevin Y. Ma,*† Pakpong Chirarattananon,† Sawyer B. Fuller, Robert J. Wood

Flies are among the most agile flying creatures on Earth. To mimic this aerial prowess in a similarly sized robot requires tiny, high-efficiency mechanical components that pose miniaturization challenges governed by force-scaling laws, suggesting unconventional solutions for propulsion, actuation, and manufacturing. To this end, we developed high-power-density piezoelectric flight muscles and a manufacturing methodology capable of rapidly prototyping articulated, flexure-based sub-millimeter mechanisms. We built an 80-milligram, insect-scale, flapping-wing robot modeled loosely on the morphology of flies. Using a modular approach to flight control that relies on limited information about the robot's dynamics, we demonstrated tethered but unconstrained stable hovering and basic controlled flight maneuvers. The result validates a sufficient suite of innovations for achieving artificial, insect-like flight.

Using flapping wings and tiny nervous systems, flying insects are able to perform sophisticated aerodynamic feats such as deftly avoiding a striking hand or landing on flowers buffeted by wind. How they perform these feats—from sensorimotor transduction to the unsteady aerodynamics of their wing motions—is just beginning to be understood (*1*–*3*), aided in part by simulation (*4*) and scaled models (*5*). Motivated by a desire for tiny flying robots with comparable maneuverability, we seek to create a robotic vehicle that mirrors these basic flight mechanics of flies. At the scale of flies, no such vehicle has been demonstrated to date because of the severe miniaturization challenges that must be overcome for an insect-sized device (*6*). Conventional technologies for macroscale aircraft propulsion and manufacturing are not viable for millimeter-scale robots because of inefficiencies that arise from force scaling, suggesting a biologically inspired solution based on flapping wings (*7*–*9*). Here, we report an aggregation of innovations in design, manufacturing, actuation, and control to create an insect-scale flying robot—a robotic fly—that successfully demonstrates tethered but unconstrained flight behavior reminiscent of flying insects.

For inspiration of form and function, we used *Diptera* (flies) as a model system because of the relative simplicity of the flight apparatus—flies by classification have only two wings—and the exemplary aerial agility that they exhibit. Dipteran flight has been well-studied (*5*, *10*–*18*), and it is understood that insect wings undergo a complex trajectory defined by three rotational degrees of freedom (*10*). This has been simplified in the robotic fly to a reciprocating flapping motion in which the wings' pitch rotation is regulated with passive compliant flexures (*19*)—an enabling simplification for mechanism design and manufacture. Key aspects of the oscillatory wing motion are the flapping frequency and wing stroke amplitude; the robotic fly achieves 120 Hz and 110°, respectively, similar to the 130-Hz wing beat

School of Engineering and Applied Sciences and the Wyss Institute for Biologically Inspired Engineering, Harvard University, Cambridge, MA 02138, USA.

*Corresponding author. E-mail: kevinma@seas.harvard.edu
†These authors contributed equally to this work.

frequency and 120°- to 150°-stroke amplitude in flies of comparable mass (*1*, *11*). The wing planform is inspired by the aspect ratio and area distribution of the hoverfly *Eristalis*, with wing area chosen to be consistent with similarly sized insects in terms of wing loading and peak wing velocities (*1*).

The mechanical components for a robotic fly require feature sizes between micrometers and centimeters—too large for silicon-based microelectromechanical systems (MEMS) and too small for conventional machining and assembly methods (*9*). Decreased feature size brings an increased dominance of surface forces, causing revolute joints or sliding surfaces to become inefficient or infeasible (*8*, *9*). Additionally, MEMS techniques, although sufficiently precise, are time-consuming, constrain material choice, and limit attainable geometries.

We developed a design and manufacturing methodology, "smart composite microstructures" (SCM), to address this void in mesoscale manufacturing (*9*). In SCM, material layers are bulk laser-micromachined and laminated together by using adhesives in a monolithic, planar fashion. Bulk micromachining results in feature sizes as small as 5 μm, and lamination allows virtually any material combination. Furthermore, the monolithic, parallel nature of this method facilitates mass production (Fig. 1A) and precision assembly through folding (*20*). All electromechanical elements of the robotic fly—including flight muscles, thorax, skeleton, and wings—were manufactured by use of SCM. Structural elements were created by using high stiffness-to-weight-ratio carbon fiber-reinforced composites, and articulation was achieved with polyimide film flexure hinges emulating low-friction revolute joints.

Flapping-wing flight is energetically costly (*1*), making power density and transduction efficiency vital metrics for flight muscle performance (*21*). Unfavorable scaling of magnetic forces limits the use of rotary electromagnetic motors (*8*, *21*), which are otherwise ubiquitous in larger robots. A survey of actuation technologies identified induced-strain materials, particularly piezoelectric ceramics, as most promising for oscillatory power delivery in insect-scale robots (*21*). Thus, for flight muscles we used voltage-driven piezoelectric bimorphs that can generate bidirectional forces, are compatible with our manufacturing methods, and are geometrically optimized for energy density (*22*).

The wing-flapping motion of the robotic fly is generated by a four-bar linkage that acts as a lever arm to amplify the small displacement of the piezoelectric flight muscle. A second degree of freedom is wing pitch rotation: This is relegated to a passive, elastic flexure hinge at the base of the wing. Inertial, aerodynamic, and elastic forces determine wing rotation as it interacts with the air (Fig. 1F) (*19*, *23*). This passive wing rotation mimics that observed in insects (*12*), although *Diptera* are known to possess additional musculature for active fine-tuning of rotation dynamics (*1*). The flapping motion, along with the passive pitch rotation of the wings, generates a downward propulsive force when averaged over a full stroke cycle. Thus, even with our design simplifications we can create wing kinematics that resemble wing motions in insect flight and generate sufficient lift forces for flight (*5*, *20*). Baseline wing kinematics are driven by sinusoidally exciting the piezoelectric flight muscle near the resonant frequency of the coupled muscle-thorax-wing system so as to minimize the energy expenditure on reactive power. Elastic energy storage in the robotic fly's flight apparatus parallels the energy storage observed in the thoracic mechanics of flies (*1*, *13*). Thrust modulation in the robot is achieved through amplitude modulation rather than frequency modulation so that the system

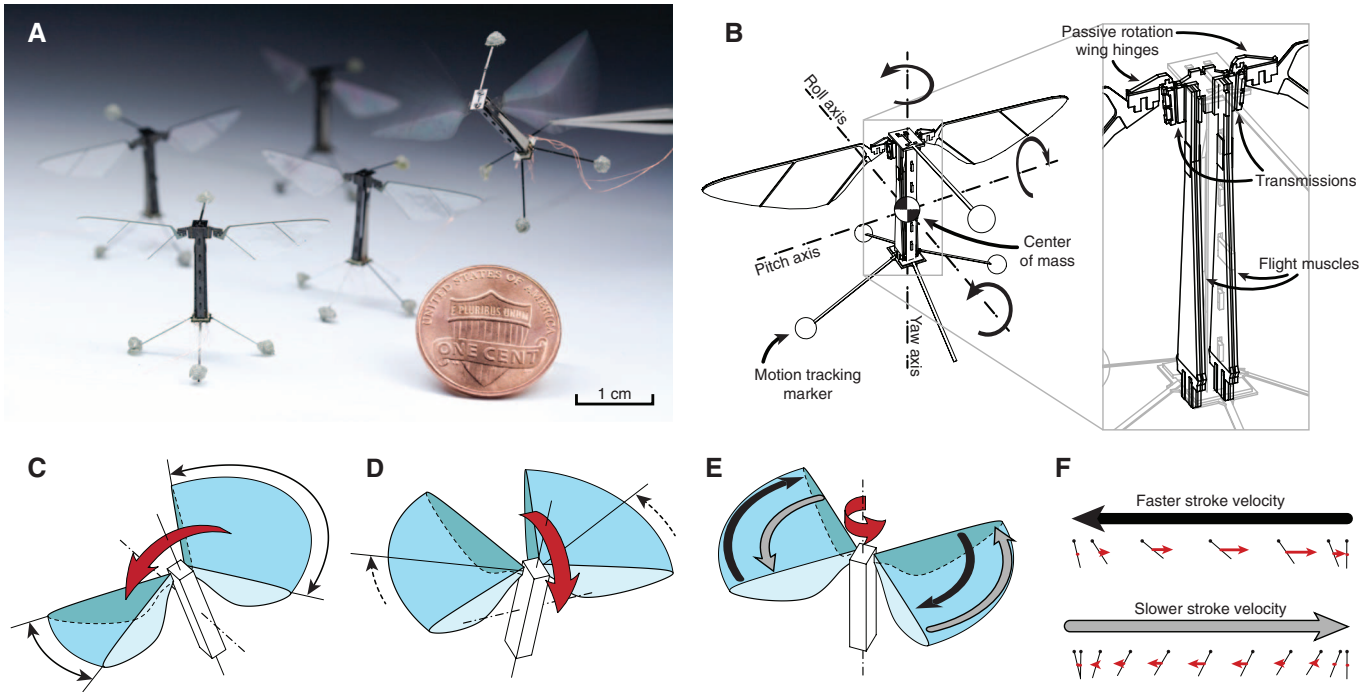

Fig. 1. A robotic fly design with a pair of independently actuated wings enables precise control of torques about three orthogonal axes. (**A**) Five individual robotic flies of identical design are shown alongside a U.S. penny for scale, demonstrating that the manufacturing process facilitates repeatability and mass production. (**B**) Body axes definitions. The inset identifies key elements of the robot design and illustrates how each wing is independently driven by a separate flight muscle. (**C**) Roll torque is generated by flapping one wing with larger stroke amplitude than the other, inducing differential thrust forces (*7*). (**D**) Pitch torque is generated by moving the mean stroke angle of both wings forward or backward to offset the thrust vector away from the center of mass. This mimics a method observed in *Drosophila* (*17*). (**E**) To generate yaw torques, the robot influences wing drag forces by cyclically modulating stroke velocity in a "split-cycle" scheme (*25*, *30*) rather than tilting the stroke plane (*10*) or altering wing angle of attack (*18*) as have been observed in *Drosophila*. A difference in stroke velocity between half-wing strokes results in an imbalanced drag force per stroke cycle—the higher velocity half-stroke (black arrow) produces greater drag force. By modulating magnitude and direction of this mean drag force on both wings, a net yaw torque is generated. The black and gray arrows correspond to arrows in (F). (**F**) The effect of stroke velocity on a wing's drag force. Black lines indicate the wings' position and pitch angle at temporally equidistant points within the stroke cycle. The red arrows indicate the instantaneous drag force on the wing.

Downloaded from www.sciencemag.org on May 3, 2013

remains at resonance (*20*). This is analogous to behavior observed in other flying insects (*1*, *24*).

The robotic fly departs from earlier single-actuator designs (*19*) by powering each wing with a separate, identical flight muscle to actuate two wings independently (*20*). This enables it to exert control torques about all three body axes (Fig. 1, B to F). The dual-actuator design weighs 80 mg, has a wingspan of 3 cm, and is capable of generating >1.3 mN of lift force (*20*). We measured power consumption of the robot to be 19 mW [which is consistent with similarly sized insects (*1*)], drawn from an offboard power source via a wire tether. If we implement onboard power with current technologies, we estimate no more than a few minutes of untethered, powered flight (*25*). Long duration power autonomy awaits advances in small, high-energy-density power sources.

Modulation of thrust force and three (approximately orthogonal) body torques (*25*) permits the robot to be controllable in unconstrained flight. To achieve stable flight, we must implement an active flight controller because, similar to flying insects, the dynamics of our insect-scale vehicle are fast and unstable (*4*, *26*), posing a difficult controller design problem reminiscent of the control of fighter jets (*27*) but analogously promising the potential for high-performance maneuverability. Sensing and controller computation are performed off-board, and power and control signals are sent to the robot via a wire tether consisting of four bundled, 51-gauge copper wires. The low mass (5 mg) and highly variable conformation of the tether suggests that it does not have a meaningful impact on the stability of the robot (*25*).

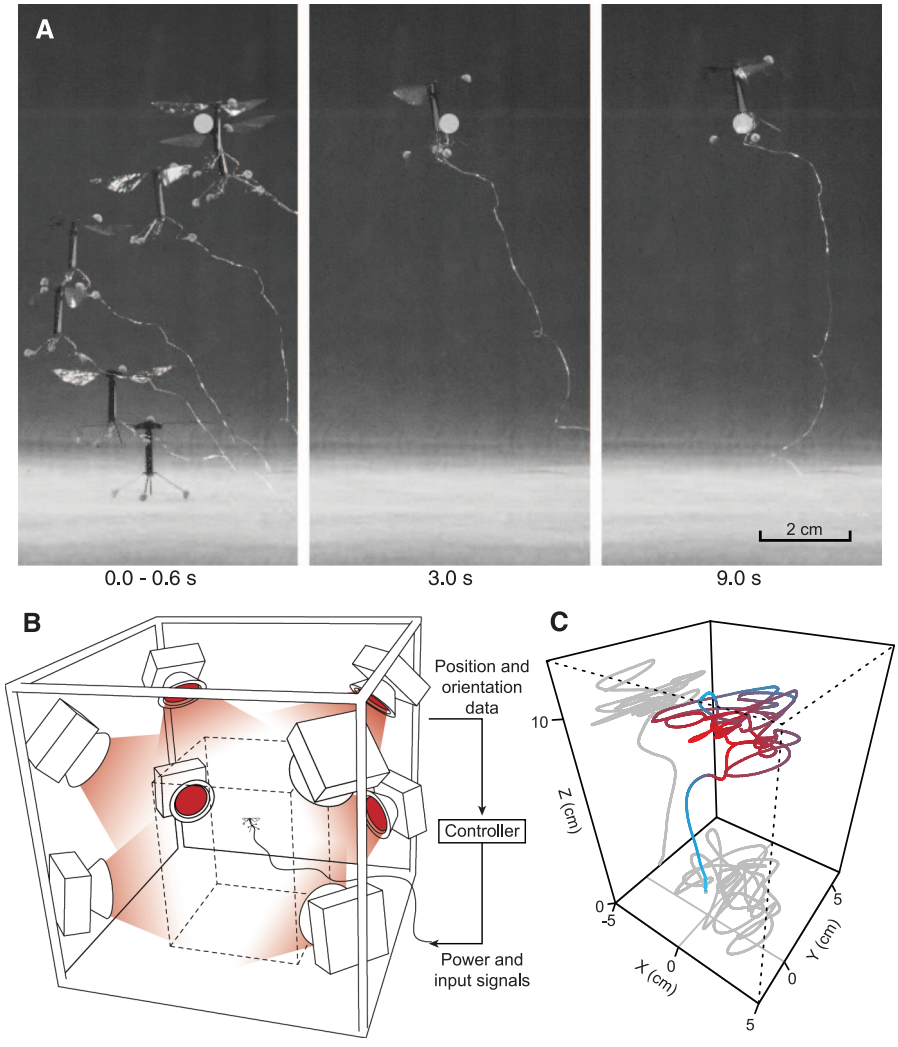

Fig. 2. Controlled takeoff and hovering of the robotic fly. (**A**) Frames from movie S1 at various times during the robot's flight. (Left) Strobed positions at 0.1-s intervals. The white dot indicates the desired hovering location. (**B**) Eight infrared, motion tracking cameras observe the positions of retroreflective markers attached to the robot in order to estimate its position and orientation in space with low latency. Position estimates are transmitted to the controller computer, which computes the control signals and sends them to the robot via a wire tether. (**C**) Three-dimensional reconstruction of the hovering flight trajectory in movie S1. Target position is 10 cm above ground. Line color gradient indicates distance from the target point, with red indicating closer proximity.

To sense the state of the robotic fly, we operated the robot in a virtual volume defined by an external array of motion-capture cameras; position and orientation were estimated by observing retroreflective tracking markers mounted on the robot (Fig. 2B). In contrast, flies appear to use dorsally oriented ocelli to estimate orientation and halteres to measure angular rates (*3*, *14*). Taking into account the sampling frequency of the motion-capture system (500 Hz), the latency of the computation, and the phase shift caused by the dynamics of the thorax, we estimated the total latency of the robotic fly's sensorimotor system to be ~12 ms (*25*). This proved to be sufficiently high bandwidth for the fast rotational dynamics of our insect-sized vehicle and is comparable with the 10-ms latency measured in the neuromotor reflexes of *Drosophila* (*15*).

Each robotic fly has distinct, unpredictable variations and asymmetries despite best efforts in manufacturing precision. Key system properties such as the flight muscle-thorax-wing system

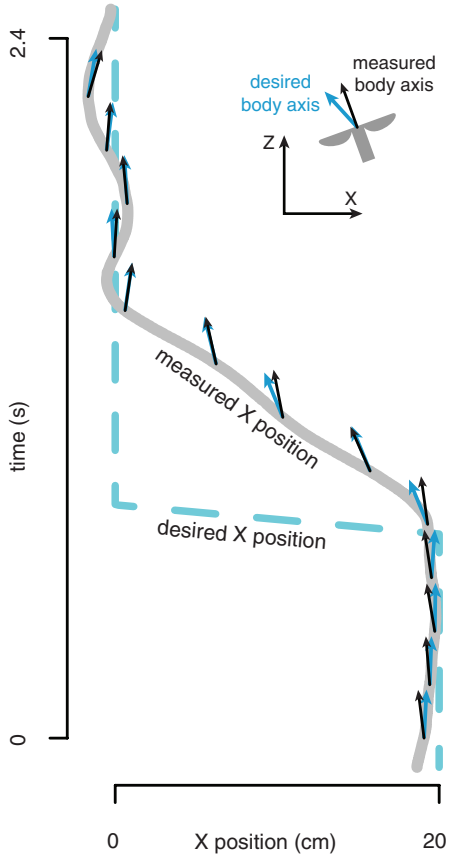

Fig. 3. The robotic fly executes a lateral maneuver (movie S2). During the maneuver, the altitude remains roughly constant. With time plotted on the vertical axis, the orientation of the robot's body axis, as projected onto the *x*-*z* plane, tilts to generate lateral forces in response to a change in the desired lateral position (dashed line). Robot orientation vectors are shown at temporally equidistant points 0.22 s apart so as to show the dynamics of the stabilization response and are not drawn to scale.

Downloaded from www.sciencemag.org on May 3, 2013

dynamics; exact magnitude, direction, and point of action of aerodynamic forces from wing trajectories; and the necessary compensation for torque biases from manufacturing inconsistencies are difficult to measure with commercially available sensors because of the small scale of the robot. Using a combination of custom-built sensors (*20*), theoretical models (*23*, *28*), and system identification during flight tests, we estimated these properties to aid in controller design (*25*).

The flight controller design consists of three distinct modules controlling body attitude, lateral position, and altitude and is subject to the constraints of the mechanical system; the stroke planes of the wings—and thus the direction of their time-averaged thrust vectors—essentially remain fixed with respect to the robot's body axis. To stay aloft, the robot must maintain a nominally upright orientation via stabilizing body torques so that its net thrust vector compensates for gravity. To induce lateral forces, the robot must reorient the body so that the net thrust vector takes on a lateral component (Fig. 3). This mimics the body tilt behavior observed in flies (*10*, *16*). Therefore, the body attitude controller module is critical. We use a Lyapunov function to derive an attitude control law that is asymptotically stable, given several simplifying assumptions (*25*). The control law consists of a proportional term that accounts for the error from a reference orientation and a derivative term that opposes angular velocity, providing rotational damping. The lateral position controller module operates by calculating the necessary reference orientation for the body attitude controller module to produce the appropriate lateral force component.

The altitude controller does not rely on information about body attitude; it is based on a linearization of the robot's dynamics at hover and assumes the system is always at an upright orientation. This decoupling of the controller allows for reduced constraints on the more sensitive attitude and lateral position controllers (*25*). In practice, the robot effectively maintains altitude because the body attitude does not deviate substantially from the nominal upright orientation, even when generating compensatory lateral forces.

In flight tests, the robotic fly demonstrated stable hovering about a fixed point with position errors on the order of one body length around the target position (Fig. 2, A and C, and movie S1), sustaining flights for longer than 20 s without ever approaching a crash. It also demonstrated lateral flight maneuvers, alternating between two fixed points in space by a switch of the target lateral position (Fig. 3 and movie S2).

Because of its scale and ability to perform stable, controlled flight, the robotic fly provides an alternative method for studying insect-scale, flapping-wing flight mechanics and flight control. For example, our flight data suggest that the robot's attitude-stabilization torques are highly dependent on information about angular velocities (Fig. 4). This coincides with the biological observation that haltere-mediated feedback is rate-dependent in *Drosophila* (*14*) and the similar finding in theoretical models of other flying insects (*26*). Additionally, flapping-wing flight experiences movement-based forces and torques that may be difficult to simulate in dynamically scaled fluid mechanics models. These dynamics, such as nonlinearities and cross-coupling of different degrees of freedom that arise during complicated flight maneuvers, could be measured with model fitting (*29*) or onboard sensors.

Even with a single actuated degree of freedom in each wing, the simplicity of the robot's mechanical design, in combination with scale-appropriate manufacturing and control strategies, is sufficient to enable controllable, insect-scale flapping-wing flight. The successful flight of the robotic fly demonstrates the feasibility of artificially approximating the flight apparatus of flying insects—particularly *Diptera*—in form and function and motivates future studies in miniaturized power, sensing, and computation technologies.

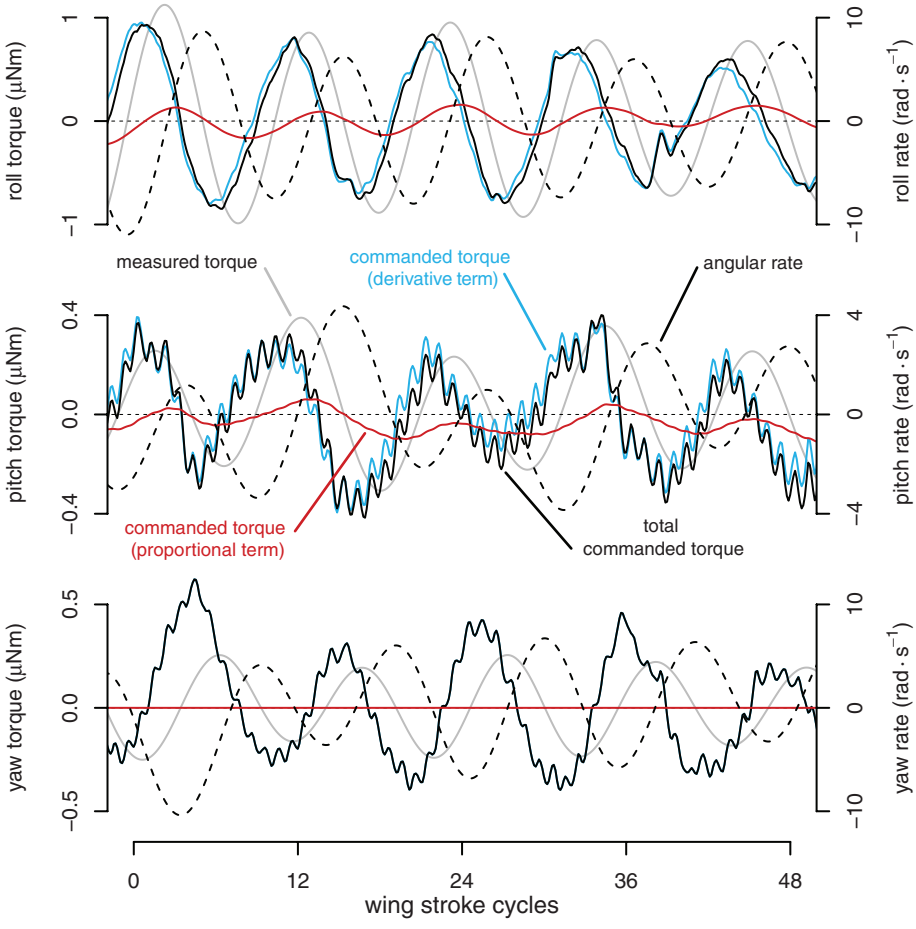

Fig. 4. Commanded torque magnitudes during an attitude-stabilized flight indicate that stabilization torques are dominated by the derivative term of the controller. In this study, lateral position control was turned off to emphasize torque commands from attitude stabilization. In the yaw torque plot, the proportional term does not contribute because, by design, only yaw rate is controlled (*25*). The commanded torque counters the measured angular rate with a delay of approximately two wing-stroke cycles. In all cases, the measured torque follows the commanded torque with a constant delay due to sensor latency and robot thoracic mechanics. Angular rate and measured torque (estimated from angular rate and the inertia of the robot) was low-pass filtered with a cutoff frequency of 60 Hz in order to reduce noise. The robot's flapping frequency is 120 Hz, and its effect can be observed as a higher-frequency oscillation superimposed on the commanded torque signals.

References and Notes

1. R. Dudley, *The Biomechanics of Insect Flight: Form, Function, Evolution* (Princeton Univ. Press, Princeton, NJ, 2002).
2. G. K. Taylor, *Biol. Rev. Camb. Philos. Soc.* **76**, 449 (2001).
3. G. Taylor, H. Krapp, *Adv. Insect Physiol.* **34**, 231 (2007).
4. C. Orlowski, A. Girard, *Prog. Aerosp. Sci.* **51**, 18 (2012).
5. M. H. Dickinson, F. O. Lehmann, S. P. Sane, *Science* **284**, 1954 (1999).
6. R. Wood *et al.*, *Int. J. Robot. Res.* **31**, 1292 (2012).
7. C. P. Ellington, *J. Exp. Biol.* **202**, 3439 (1999).
8. W. Trimmer, *Sens. Actuators* **19**, 267 (1989).
9. R. Wood, S. Avadhanula, R. Sahai, E. Steltz, R. Fearing, *J. Mech. Des.* **130**, 052304 (2008).
10. S. N. Fry, R. Sayaman, M. H. Dickinson, *Science* **300**, 495 (2003).
11. A. Ennos, *J. Exp. Biol.* **142**, 49 (1989).
12. A. Ennos, *J. Exp. Biol.* **140**, 161 (1988).
13. M. Dickinson, M. Tu, *Comp. Biochem. Physiol. A* **116**, 223 (1997).
14. M. H. Dickinson, *Philos. Trans. R. Soc. Lond. B Biol. Sci.* **354**, 903 (1999).
15. L. Ristroph *et al.*, *Proc. Natl. Acad. Sci. U.S.A.* **107**, 4820 (2010).

Downloaded from www.sciencemag.org on May 3, 2013

16. C. T. David, *Physiol. Entomol.* **3**, 191 (1978).
17. J. M. Zanker, *Physiol. Entomol.* **13**, 351 (1988).
18. A. J. Bergou, L. Ristroph, J. Guckenheimer, I. Cohen, Z. J. Wang, *Phys. Rev. Lett.* **104**, 148101 (2010).
19. R. Wood, *IEEE Trans. Robot.* **24**, 341 (2008).
20. K. Ma, S. Felton, R. Wood, "Design, fabrication, and modeling of the split actuator microrobotic bee," 2012 IEEE/RSJ International Conference on Intelligent Robots and Systems, Vilamoura, Algarve, Portugal, 7–12 October 2012, pp. 1133–1140.
21. M. Karpelson, G. Wei, R. Wood, "A review of actuation and power electronics options for flapping-wing robotic insects," 2008 IEEE International Conference on Robotics and Automation, Pasadena, CA, USA, 19–23 May 2008, pp. 779–786.
22. R. Wood, E. Steltz, R. Fearing, *Sens. Actuators A Phys.* **119**, 476 (2005).
23. J. Whitney, R. Wood, *J. Fluid Mech.* **660**, 197 (2010).
24. D. L. Altshuler, W. B. Dickson, J. T. Vance, S. P. Roberts, M. H. Dickinson, *Proc. Natl. Acad. Sci. U.S.A.* **102**, 18213 (2005).
25. Materials and methods are available as supplementary materials on *Science* Online.
26. B. Cheng, X. Deng, T. L. Hedrick, *J. Exp. Biol.* **214**, 4092 (2011).
27. M. Abzug, E. Larrabee, *Airplane Stability and Control: A History of the Technologies that Made Aviation Possible* (Cambridge Univ. Press, Cambridge, UK, 2005).
28. B. Finio, N. Pérez-Arancibia, R. Wood, "System identification and linear time-invariant modeling of an insect-sized flapping-wing micro air vehicle," 2011 IEEE/RSJ International Conference on Intelligent Robots and Systems, San Francisco, CA, USA, 25–30 September 2011, pp. 1107–1114.
29. W. Hoburg, R. Tedrake, System identification of post stall aerodynamics for UAV perching. *Proc. AIAA Infotech Aerospace Conf.* (AIAA, Seattle, WA, 2009).
30. M. Oppenheimer, D. Doman, D. Sigthorsson, Dynamics and control of a biomimetic vehicle using biased wingbeat forcing functions: Part I—Aerodynamic model. *Proc. 48th AIAA Aerospace Sci. Meeting* (AIAA, Orlando, FL, 2010).

Acknowledgments: This material is based on work supported by the National Science Foundation under grant CCF-0926148, the Office of Naval Research under grant N00014-08-1-0919, and the Wyss Institute for Biologically Inspired Engineering. Any opinions, findings, and conclusions or recommendations expressed in this material are those of the authors and do not necessarily reflect the views of the National Science Foundation.

Supplementary Materials

www.sciencemag.org/cgi/content/full/340/6132/603/DC1
Materials and Methods
Supplementary Text
Figs. S1 and S2
Table S1
References (*31*, *32*)
Movies S1 and S2

22 October 2012; accepted 12 February 2013
10.1126/science.1231806

3D Reconstruction of the Source and Scale of Buried Young Flood Channels on Mars

Gareth A. Morgan,[1]* Bruce A. Campbell,[1] Lynn M. Carter,[2] Jeffrey J. Plaut,[3] Roger J. Phillips[4]

Outflow channels on Mars are interpreted as the product of gigantic floods due to the catastrophic eruption of groundwater that may also have initiated episodes of climate change. Marte Vallis, the largest of the young martian outflow channels (<500 million years old), is embayed by lava flows that hinder detailed studies and comparisons with older channel systems. Understanding Marte Vallis is essential to our assessment of recent Mars hydrologic activity during a period otherwise considered to be cold and dry. Using data from the Shallow Radar sounder on the Mars Reconnaissance Orbiter, we present a three-dimensional (3D) reconstruction of buried channels on Mars and provide estimates of paleohydrologic parameters. Our work shows that Cerberus Fossae provided the waters that carved Marte Vallis, and it extended an additional 180 kilometers to the east before the emplacement of the younger lava flows. We identified two stages of channel incision and determined that channel depths were more than twice those of previous estimates.

The majority of outflow channels on Mars are attributed to megafloods caused by the catastrophic release of groundwater. The most prominent outflow channels, located around the Chryse Basin, are >1000 km long and are estimated to be Hesperian [~3.7 to 3.1 billion years ago (Ga)] in age (*1*–*3*). Marte Vallis in Elysium Planitia is the largest of the young (late Amazonian: ~0.5 Ga to the present) outflow channels on Mars. The channel system extends over ~1000 km in length and ~100 km in width, making Marte Vallis comparable in scale to the Chryse basin channel systems. Young lava flows have fully embayed the most elevated portions of Marte Vallis, and as a consequence the fundamental characteristics of the channels, including their source, depth, and morphology are less well understood than those of the Hesperian channels (*4*), despite being over 2.6 billion years younger (*5*).

Two possible sources have been proposed for Marte Vallis: water flowing from the Athabasca Valles outflow channel in the west (*4*, *6*, *7*), possibly forming bodies of water such as the putative frozen central Cerberus sea (*8*); and water flowing from a now-buried section of Cerberus Fossae (*5, 6, 9*). It is impossible to resolve which of the above hypotheses are correct from investigations of the surface geology alone. Using data from the Shallow Radar (SHARAD) sounder (*10*, *11*) on the Mars Reconnaissance Orbiter, we present a tomographic visualization of the buried Marte Vallis channels (*12*).

All 58 SHARAD tracks covering the uppermost reaches of Marte Vallis [as identifiable in Mars Orbiter Laser Altimeter (MOLA) gridded data] display multiple reflecting horizons (Fig. 1 and fig. S1). From mapping of the spatial distribution of SHARAD subsurface returns (Figs. 1 and 2), three distinct reflectors have been identified. Two of these reflectors are found extensively across the study area and occupy different depth ranges (*13*), referred to here as L1R (the shallower reflector) and L2R (the deeper reflector). The third reflector, R3, is located only in the southern portion of the region (Fig. 1C).

Radargrams reveal that the northern and southern termini of the R3 reflector dip upward and reconnect with the surface, delineating a discrete facies boundary (Fig. 1A and fig. S1). The R3 reflector is located exclusively below a mapped unit of young volcanics, ACy [(*5*), also mapped as AEc_3 by (*14*)] (Fig. 2C and fig. S2C). This unit is interpreted to be formed of voluminous lava flows <230 million years old (*5*, *14*), suggesting that R3 represents the base of a distinct surficial flow. The bases of young lava flows have also been identified by SHARAD west of Ascraeus Mons (*15*). The northern boundary of R3 shows strong spatial correlation with the boundary between ACy and the older unit ACo [>500 million years old (*5*)] (Fig. 2), implying that the lava embayed the preexisting ACo surface south of Cerberus Fossae and flowed toward the northeast (the dominant slope direction of the present surface). The northern portion of the R3 reflector exhibits prominent depressions, delineating subsurface channels (Fig. 1A). These channel features are ~20 km wide and extend for at least 50 km in a northeast direction. Seen in plan form, the channel features begin abruptly adjacent to one another along an orientation trending from northwest to southeast (Fig. 2C and fig. S3).

We interpret these features to be the highest elevated channels of Marte Vallis (Fig. 3), implying that the lava flow whose base is defined by R3 infilled the channels as the lavas flowed to the northeast. This indicates that the erosion of the outflow channel cut into the original underlying surface of unit ACo before the emplacement of the younger ACy lavas (fig. S4). This sequence of events confirms the young age of Marte Vallis and places the channel formation between the emplacement of units ACo and ACy [10 to 500 million years ago (Ma)], in agreement with (*5*).

The L1R and L2R reflectors are found extensively across the study region, suggesting that they represent regional boundaries between three

[1]Center for Earth and Planetary Studies, Smithsonian Institution, Washington, DC, USA. [2]NASA Goddard Space Flight Center, Greenbelt, MD 20771, USA. [3]Jet Propulsion Laboratory, Pasadena, CA, USA. [4]Planetary Science Directorate, Southwest Research Institute, Boulder, CO, USA.

*Corresponding author. E-mail: morganga@si.edu

Downloaded from www.sciencemag.org on May 3, 2013